Key Points:
- Multiannual InSAR observations of ground movement related to permafrost activity through the entire seasonal cycle over 60,000 km^2 in Tibet
- Amplitude of warm season subsidence patterns associated with active layer thawing correlate with Cenozoic sedimentary basins
- Water/ice content in permafrost active layer controls amplitude and timing of maximum subsidence

Supporting Information:
- Supporting Information S1
- Supporting Information S2

Large-scale InSAR monitoring of permafrost freeze-thaw cycles on the Tibetan Plateau

Simon Daout[1] iD, **Marie-Pierre Doin[1]**, **Gilles Peltzer[2,3]** iD, **Anne Socquet[1]** iD, and **Cécile Lasserre[1]** iD

[1]ISTerre, Université Grenoble-Alpes, CNRS, Grenoble, France, [2]Department of Earth Science, University of California, Los Angeles, California, USA, [3]Jet Propulsion Laboratory, California Institute of Technology, Pasadena, California, USA

Abstract Multitemporal interferometric synthetic aperture radar (InSAR) observations are used to characterize spatial variations of the permafrost active layer and its temporal evolution in Northwestern Tibet. We develop a method to enhance InSAR performances for such difficult terrain conditions and construct an 8 year timeline of the surface deformation over a 60,000 km^2 area. The ground movement induced by the active layer's response to climate forcing is limited to Cenozoic sedimentary basins and is spatially variable in both its seasonal amplitude (2.5–12 mm) and multiannual trend (−2 to 3 mm/yr). A degree-day integrated model adjusted to the data indicates that subsidence occurs when the surface temperature exceeds zero (May to October) over areas where seasonal movements are large (>8 mm). The period of subsidence is delayed by 1–2 months over areas where smaller seasonal movements are observed, suggesting an unsaturated soil where water occurs in the deeper part of the active layer.

1. Introduction

Permafrost, occurring where the mean ground temperature is below 0°, occupies a large fraction (20–25%) of the Earth's continental surface [*Brown et al.*, 2000; *French et al.*, 2007]. It is of fundamental importance in various domains: as an impermeable and hard layer, it controls ground moisture and water transport, evaporation, vegetation growing, and evapotranspiration. It also affects the ground thermal budget through freezing/ thawing, latent heat, and conductivity effects [*Outcalt et al.*, 1990]. Finally, it is a major reservoir of water and organic matter that decays into greenhouse gases such as carbon dioxyde and methane [*Christensen et al.*, 2004]. The complex interactions and feedback between increased air temperature, ground temperature, and permafrost evolution must be taken into account in climate models [*Oelke and Zhang*, 2007; *Cheng and Wu*, 2007; *Riseborough et al.*, 2008].

The upper layer of the permafrost is subject to seasonal freezing and thawing. It is strongly deforming and cracking due to the volume change associated with water ice phase changes in pores and lenses of its active layer, leading to the development of characteristic geomorphic patterns defining circle or polygon-shape cracks, palsas, and pingos. The thickness of the active layer (ALT) and the quantity of water/ice stored in it varies spatially and interannually, scaling with the amplitude of the ground displacement. Ground cohesion and movement affect infrastructure stability (e.g., buildings foundations and railways [*Qingbai et al.*, 2002; *Chang and Hanssen*, 2015]) and thus the socioeconomic development of the area. Inferring the active layer properties from air temperature is a difficult exercise as it depends on local thermal properties, snow cover, soil layering and water availability [*Smith and Riseborough*, 1996]. The ALT is usually measured "in situ" by probing [*Zorigt et al.*, 2016; *Cheng and Wu*, 2007] or through geophysical investigations such as temperature sensors or ground penetrating radar [*Hinkel et al.*, 2001; *Wu et al.*, 2010]. Estimating ALT variations over broad regions can be done by interpolating probe data using vegetation index maps compiled from remotely sensed data [*Nelson et al.*, 1997], ground resistivity [*Pastick et al.*, 2013], or relative elevation [*Gangodagamage et al.*, 2014]. However, in situ measurements are sparse, making their interpolation inaccurate. Hence, the systematic mapping of ground movements observed by interferometric synthetic aperture radar (InSAR) over broad areas should provide unprecedented insights into characterizing permafrost active layer properties in many regions.

Multitemporal radar interferometry (MT-InSAR) in natural environment [*Hooper et al.*, 2004; *Berardino et al.*, 2002] is providing new opportunities to map and measure these seasonal surface displacements, as it has been shown on relatively limited spatial extent in Alaska [e.g., *Liu et al.*, 2010; *Short et al.*, 2011; *Liu et al.*, 2012,

2014, 2015; *Schaefer et al.*, 2015] or in Tibet [e.g., *Chang and Hanssen*, 2015]. However, over broad areas, the approach suffers from major limitations including decorrelation created by cryoturbation of the surface or snow cover, strong phase gradients leading to unwrapping errors, and temporal decorrelation. Previous InSAR studies of permafrost behavior have identified these challenges but circumvent the problem by focusing on small areas (<5000 km^2) and sometimes, because of snow cover, using only acquisitions acquired during the thawing season. In this paper, we show that MT-InSAR data can be used to retrieve the permafrost related deformation through the entire seasonal cycle over a wide area ($\sim$240 $\times$ 250 km^2) with a high spatial and temporal resolution. The demonstration is done on the northwestern part of the Tibetan plateau where permafrost occupies around 70% of the land [*Brown et al.*, 2000]. With an average elevation of $\sim$5 km, the study area is covered with a succession of east-west trending, flat sedimentary basins, separated by narrow mountain ranges reaching 6 km in height, leading to an extensive zone of discontinuous permafrost [*Fort and van Vliet-Lanoe*, 2007].

In the following sections, we first describe how we process single interferograms and improve phase unwrapping across permafrost areas. The interferograms are then combined to construct a timeline of ground movement maps covering 8 years. Finally, we discuss observed cross correlations between observable parameters and possible implications for processes involved in the freeze-thaw cycle and permafrost evolution.

2. Data Processing

We process the complete Envisat data archive along four $\sim$240 km long and 100 km large overlapping descending tracks (162, 391, 119, and 348) between 2003 and 2011 (Insert Figure 1). To construct deformation time series, we use the New Small Baselines Subset (NSBAS) chain [*Doin et al.*, 2011, 2015] based on the ROI_PAC software [*Rosen et al.*, 2004]. The networks of the 495 interferograms are shown in Figures S1 and S2 and Table S1 in the supporting information.

Before the critical step of phase unwrapping, which is prone to many errors, we apply three important corrections to the wrapped phase of all interferograms in order to improve the data signal-to-noise ratio. (1) We remove the phase delay based on an Atmospheric Phase Screen (APS) using the global atmospheric reanalysis model, ERA-Interim [*Dee et al.*, 2011; *Doin et al.*, 2009; *Jolivet et al.*, 2011] (Figures S3b and S4). As we are here at an elevation of $\sim$5000 m in a dry environment, turbulent APS is moderate with respect to what could be seen at lower elevation (Figure S4). (2) We then estimate a linear term in range to remove the residual orbital errors and the effect of the clock drift [*Fattahi and Amelung*, 2014; *Zhang et al.*, 2014] (Figure S3c). (3) We correct the effect of digital elevation model (DEM) errors [*Ducret et al.*, 2014] (Figure S3d). These corrections significantly reduce the noise on the wrapped phase for further processing [e.g., *Grandin et al.*, 2012; *Daout et al.*, 2016]. However, we observe in the corrected phase several zones of narrow deformation and phase discontinuity, sometimes exceeding half a cycle, near the edge of sedimentary basins, making phase unwrapping difficult in these areas (Figs S3d, S7a and S7b, and S8a). These patterns are principally observed on interferograms built from pairs of images acquired at different seasons.

In order to unwrap the phase with confidence across the edges of sedimentary basins in all interferograms, we implement an iterative unwrapping procedure by removing from the phase a template of the deformation signal based on the principal component analysis (PCA) of a first subseries of correctly unwrapped interferograms (see supporting information Figures S5 and S6) [e.g., *Strozzi and Wegmuller*, 1999; *Yun et al.*, 2007; *Pinel et al.*, 2008; *López-Quiroz et al.*, 2009]. After the unwrapping of the reduced phase (Figures S7c, S7d, and S8b), the template is added back to each interferogram to reconstruct the full unwrapped phase signal (Figure S7e).

The series of unwrapped interferograms is then inverted to construct a timeline of LOS displacement maps [*Doin et al.*, 2015] (Figure S9a). To avoid any confusion with the long wavelength tectonic signal, the ground displacement in the basins is referenced to the bedrock as defined by the PCA template (Figure S10).

3. Results and Discussions

The multiannual displacement of the ground in the sedimentary basins is dominated by a seasonal signal corresponding to ground upheaval in winter and spring and subsidence in summer and autumn (Figure S9a). We adjust a sine function plus a linear trend to the 2003–2011 displacement data of each image pixel (Figure S9b) to estimate the average amplitude of the seasonal signal (Figure 1), the month of the maximum subsidence
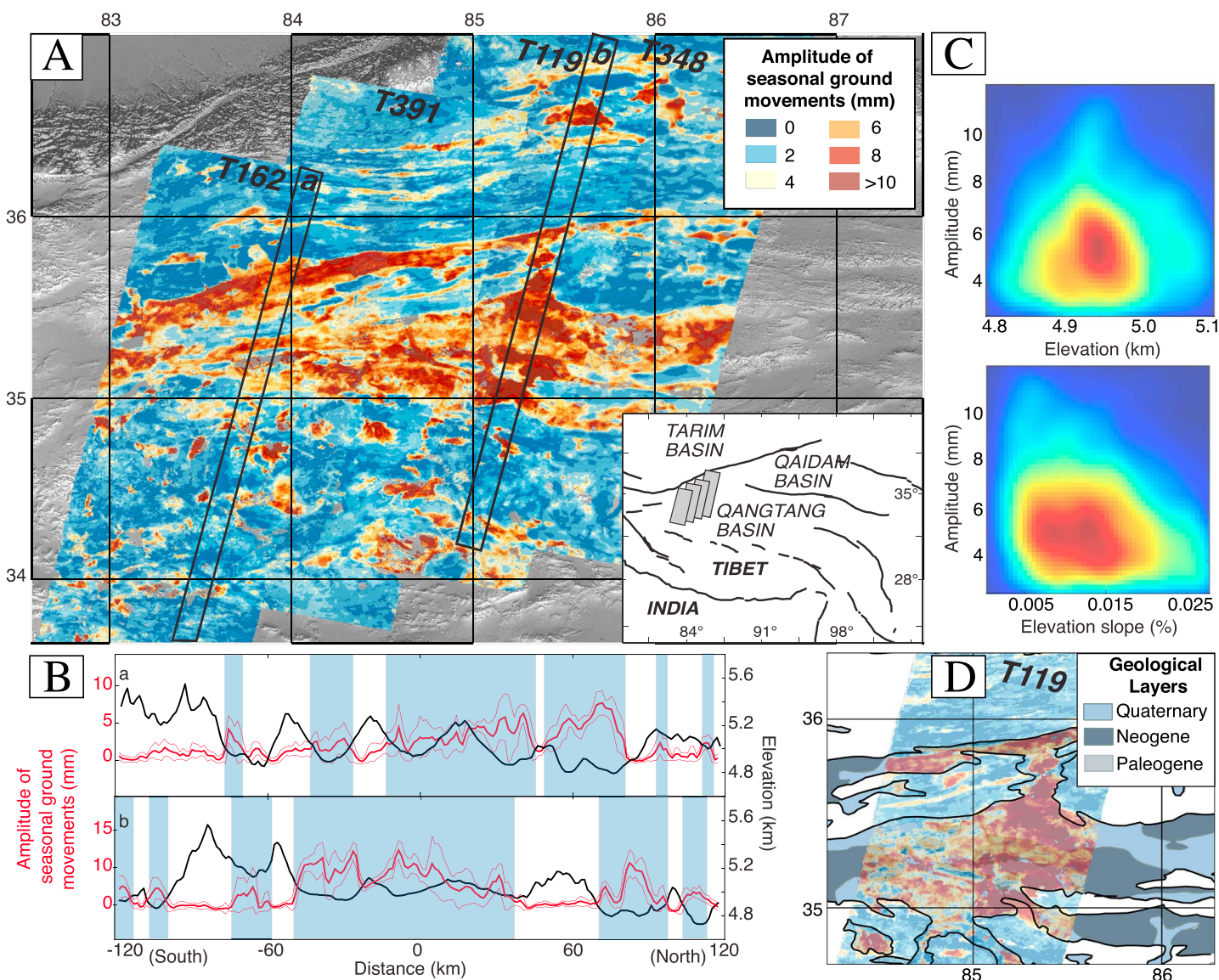
Figure 1. (a) Map of the amplitude of the seasonal ground movements extracted from InSAR time series analysis of four independent tracks, superimposed on the elevation Shuttle Radar Topography Mission (SRTM). Bottom right inset: location of the four tracks acquired along descending orbits. (b) Profiles of amplitude of seasonal deformation and elevation along tracks 162 (a) and 119 (b). Areas where seasonal signal is larger than 2.5 mm are emphasized by light blue shade and correspond to valleys. (c) Density plots showing the correlation between amplitude of the seasonal movements and elevation or terrain elevation slope. (d) Zoom on the amplitude of the seasonal deformation for track 119 superimposed on the geological map [*Pan et al.*, 2004].

(Figure 2), and the multiannual ground velocity (Figure 4). Independent estimates of these quantities in areas of overlap between adjacent satellite tracks indicate a remarkable consistency in map view as confirmed by the small associated uncertainties (Figure S11 in the supporting information). A sinusoidal function offers a first-order, linear fit to the data and is used here to map lateral variations of the amplitude of the seasonal signal and the time of the maximum subsidence. We also discuss a more physical model based on the degree day integrated over the freezing and thawing periods [*Stefan*, 1891].

3.1. Amplitude of the Seasonal Ground Movements

The amplitude of the seasonal signal ranges between 0 mm and 12 mm with uncertainties lower than 1.5 mm (Figures 1a and S11a). The arid climate of Tibet and the short period of positive temperatures explain the relatively small amplitude compared to places like Alaska where the seasonal signal reaches up to 4 cm [e.g., *Liu et al.*, 2010]. Zones where the average amplitude of the seasonal signal exceeds 2.5 mm coincide with the narrow and elongated basins between the east-west mountain ranges (Figures 1a, 1b, and S12a).
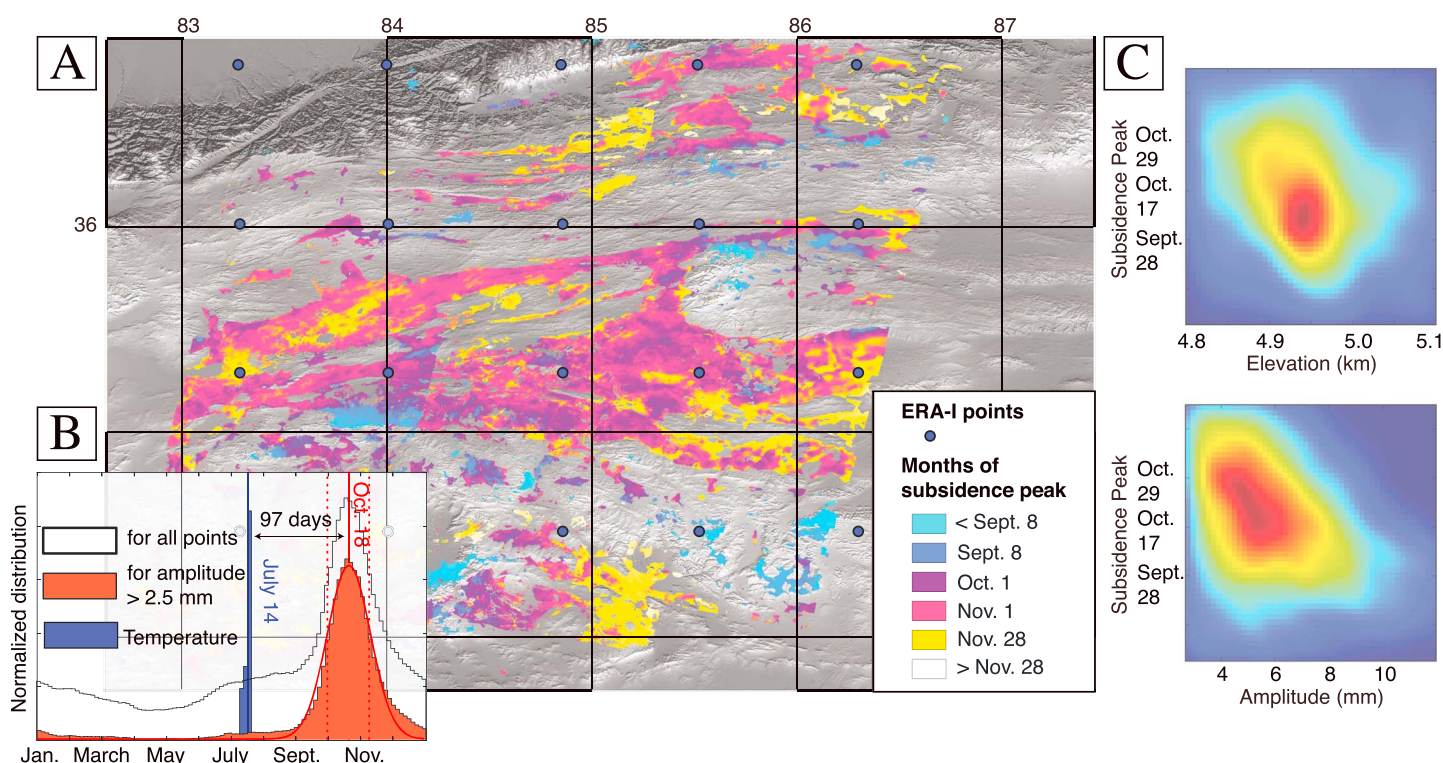
Figure 2. (a) Month of the seasonal subsidence peak (maximum subsidence) superimposed on shaded elevation (SRTM). We only show points for which the seasonal amplitude is greater than 2.5 mm. Blue dots display the ERA-Interim (ERA-I) atmospheric grid used in this study. (b) Histograms of date of subsidence peak for all pixels (white) and for pixels affected by a seasonal deformation grater than 2.5 mm (red) compared to that of temperature maxima derived from European Center for Medium range Weather Forecasting model at all ERA-I points. (c) Density plots showing the correlation between the date of subsidence peak and elevation or the amplitude of the seasonal movements.

The ruggedness of the terrane computed using the SRTM elevation data highlights the flat sedimentary basins in and around our study area (Figure S12b). The boundaries of the basins match almost perfectly the 2.5 mm contour of the displacement map (Figures 1d and Figure S12c). The superimposition of amplitude on the Google Earth imagery further indicates the detailed correspondence with the sedimentary basins (Figure S12d). The upper layer of the sedimentary basins is mostly composed of unconsolidated material ranging from fine silt to coarser gravel sediments and conglomerates emplaced in alluvial fans [*Pan et al.*, 2004]. The high porosity of these sediments compared to bedrock implies a large water storage capacity resulting in ground deformation during the freeze-thaw cycle.

The spatial variability of the amplitude of the seasonal deformation is controlled by the water content and thermal properties of the ground upper layer and ultimately by spatial variations of the ALT. The ALT should decrease with decreasing mean temperature or cumulative thawing degree day (DDT) as the elevation increases [*Riseborough et al.*, 2008]. A negative correlation between the amplitude of the seasonal signal and the elevation could thus be expected. Although a negative correlation may be apparent in the dense part of the amplitude-elevation scatterplot (Figure 1c), the amplitude of the signal does not show a systematic dependence to elevation. In addition, the amplitude of the seasonal movement is large on flat surfaces and decreases on slopes where less water is permanently stored compared to the center of basins (Figure 1c). These observations suggest that the amplitude of the seasonal movements is mostly controlled by the moisture content in the soils of sedimentary basins [*Fort and van Vliet-Lanoe*, 2007]. Assuming a 9% expansion coefficient for the water ice phase change, a 1 m column of porous sediments containing 10% of water would raise the ground by 9 mm, within the range of observed values in the Tibetan basins. A moderate porosity of 3–12% corresponds to high gravel content whereas higher volumetric water content can be found in silts or clays [*Liu et al.*, 2014; *Schaefer et al.*, 2015]. The bedrock, however, has a very low porosity and is thus not significantly deformed through the freeze-thaw cycle.

3.2. Months of Subsidence Peak

The maximum subsidence (end of the ice thawing period) for areas of high seasonal deformation (above 2.5 mm) (Figure 2a) is observed between September and November with uncertainties typically less than 15 days (Figure S11b). The histogram (Figure 2b) shows a slightly skewed distribution, peaking on 18 October. Few patches with outlier values and amplitude lower than 4 mm (in red in Figure 2a) are concentrated in rugged terranes. The timing of maximum subsidence for low amplitude signal (below 2.5 mm) has a relatively homogeneous distribution and is considered as nonsignificant and influenced by residual atmospheric delays or noise. Air temperature extracted from ERA-I reanalysis, if fitted by a sinusoid, is maximum on 14 July, thus 97 days before the observed active layer thawing maximum (Figure 2b). This maximum is thus delayed at the very end of the warm season.

Maximum ground subsidence occurs when the whole active layer has thawed, so when the temperature is maximum at depth. This maximum is delayed with respect to the surface ground temperature due to downward heat diffusion time. Assuming an equality between surface and ground temperatures, the subsidence lag in a purely diffusive model is proportional to seasonal amplitude of the surface temperature, T_a and to the mean annual air temperature, MAAT, such as [*Anderson and Anderson*, 2010]: lag (in day) $= -365/2\pi \times \ln(-\mathrm{MAAT}/T_a)$, increasing linearly with ALT. For instance, at an elevation of 5085 m in our study area (35.25°N–86.25°E), $T_a = 11.2°$ and MAAT $= -7.3°$ (Figure 3a) imply a lag of 25 days between surface temperature and melting maxima. The measured time lag of 95 ± 20 days between air temperature and subsidence maxima is much larger than the lag predicted by a purely diffusive model.

The difference between surface air temperature and ground temperature depends on the absorption of solar radiation, the lithology, the snow cover in winter, and the vegetation in summer [*Lunardini*, 1991; *Smith and Riseborough*, 1996]. Moreover, in presence of freezing and thawing of significant amounts of soil moisture, the release and absorption of the latent heat of fusion of the soil water dominates the ground heat budget [*Riseborough et al.*, 2008]. To help understanding its spatial variations, we correlate the lag time of maximum subsidence with the elevation and the amplitude of the seasonal movement. We first observe a slight anticorrelation between the maximum subsidence lag and the elevation (Figure 2c), which may be partially explained by a shortening of the warm season, and thus a decrease of the ALT with increasing elevation. Second, areas of large seasonal amplitude correspond to an early thawing period with a maximum subsidence occurring in October compared to those of low amplitude with a maximum subsidence in November (Figure 2c).

To explain this observation and better characterize the seasonal deformation pattern, we compute the detrended and normalized seasonal signal as follows: $\phi_{\mathrm{seas}}(t) = (\mathrm{d}(t) - Vt)/A$, where $\mathrm{d}(t)$ is InSAR measurements, V is the multiyear linear trend, and A the amplitude of the seasonal deformation. Figure 3b shows the median and the standard deviation of the 12 month wrapped seasonal signal at each acquisition time. We distinguish between pixels with low amplitude ($2.5\,\mathrm{mm} < A < 8\,\mathrm{mm}$) and those with high amplitude ($A > 8$ mm) to separate slope from flat terrains. Note that there is no ground movement in the winter time when the active layer is entirely frozen, a marked departure from the simplistic sinusoid curve. To better describe the seasonal behavior of the active layer, we compute a deformation model, which is — by interval — proportional to the square root of the cumulative degree day of thawing (DDT) or freezing and constant during the time where the active layer is entirely frozen [*Harlan and Nixon*, 1978; *Leppäranta*, 1993]. In contrast with previous studies [e.g., *Liu et al.*, 2012, 2014, 2015; *Schaefer et al.*, 2015], our observations cover the full season cycle over the course of 8 years allowing us to accurately estimate the model parameters (Figure 3b, see supporting information).

Over areas of large seasonal amplitude movements, the ground starts to subside in mid-May, shortly after the surface temperature passes over 0°C and ends subsiding in mid-October, about 2 weeks after the surface temperature returns to freezing (Figure 3). This pattern suggests a saturated soil in which the water is stored up to a shallow depth bellow the surface. In contrast, over areas of moderate seasonal amplitude movements, the subsidence period appears to be delayed by 1–2 months compared to areas of larger movements (Figure 3). There, the subsidence starts in mid-July, approximately when the surface air temperature reaches its maximum and ends subsiding in late November, well into the freezing season at the surface. This pattern can be explained by a nonsaturated soil in which the ground water is stored in the bottom part of the active layer, therefore responding later to the freezing and thawing downward progressing fronts.

These findings also explain the observed anticorrelation between amplitude and phase of the ground movements (Figure 2c), a pattern that cannot be explained by a diffusive model in a homogeneous medium.
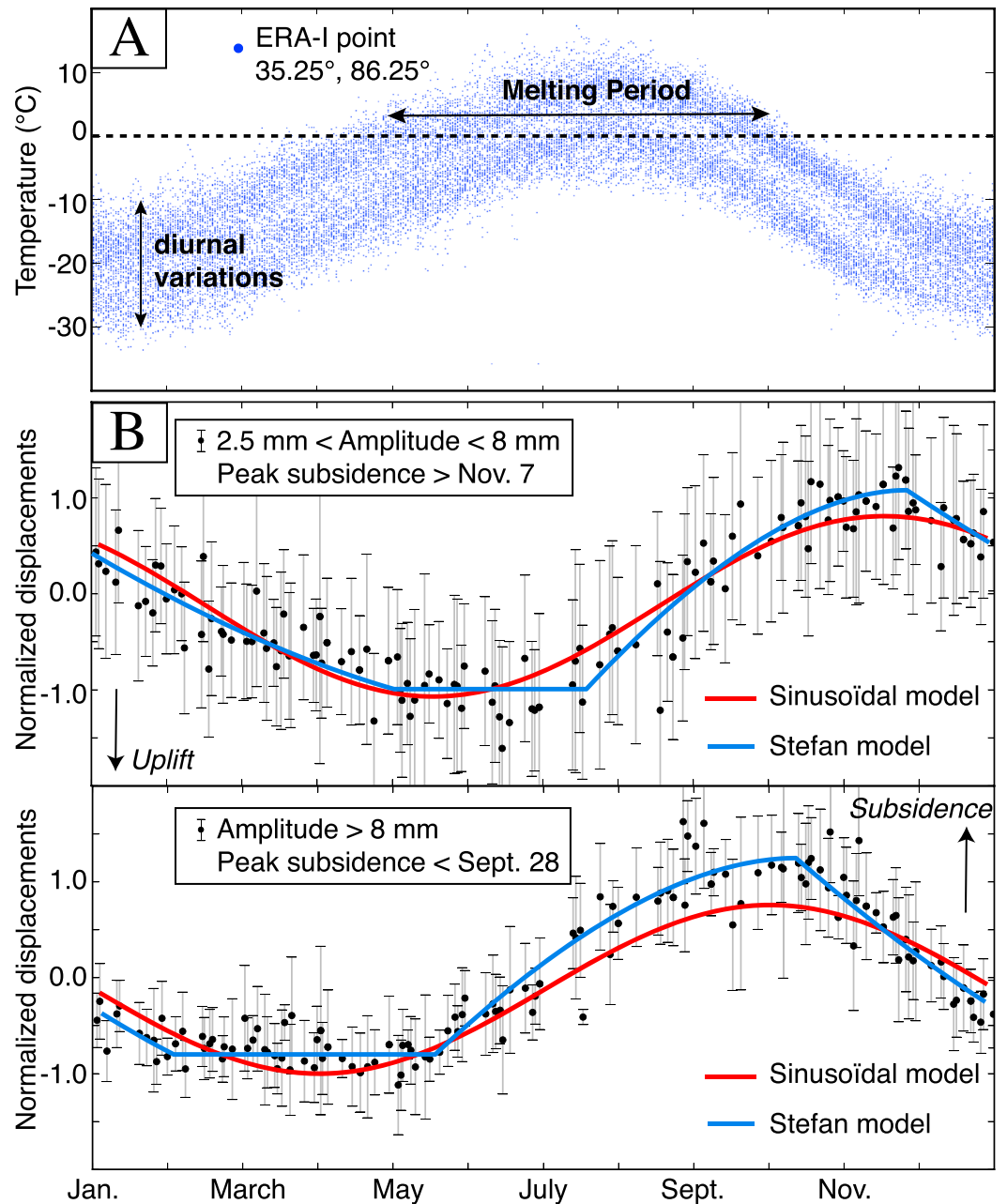
Figure 3. (a) Time series of air (2 m surface) temperature for one ERA-I point. (b) Normalized seasonal evolution at data acquisition times over study area. Top graph shows pixels with seasonal movement amplitude between 2.5 and 8 mm and bottom graph amplitude is greater than 8 mm. Superimposed curves are predictions of sinusoidal and Stefan models adjusted data (see text). Adjusted coefficients of Stefan model are $t_c = 26$ May, $t_1 = 19$ July, $t_2 = 24$ November, $c = -1.0$ mm , $A_t = 1.6$ mm (yr °)$^{-1/2}$, $A_f = 0.8$ mm(yr °)$^{-1/2}$ (top), and $t_c = 10$ February, $t_1 = 19$ May, $t_2 = 12$ October, $c = -0.8$ mm , $A_t = 1.5$ mm (yr °)$^{-1/2}$, $A_f = 1$ mm (yr °)$^{-1/2}$ (bottom).

The aridity of the climate prevailing in northwestern Tibet and the topography of the terrain result in a spatially uneven distribution of ground water, which in turn controls the distribution and behavior of the permafrost active layer [*Fort and van Vliet-Lanoe*, 2007].

3.3. Multiannual Trend of Ground Subsidence

The multiannual trend of the ground LOS velocity, restricted to areas of high seasonal deformation amplitude (>2.5 mm), is low and ranges from −2 to 3 mm/yr with isolated areas subsiding up to 4 mm/yr (Figure 4a). Uncertainties are lower than 0.5 mm/yr for all pixels, except in track 348, which includes less acquisitions
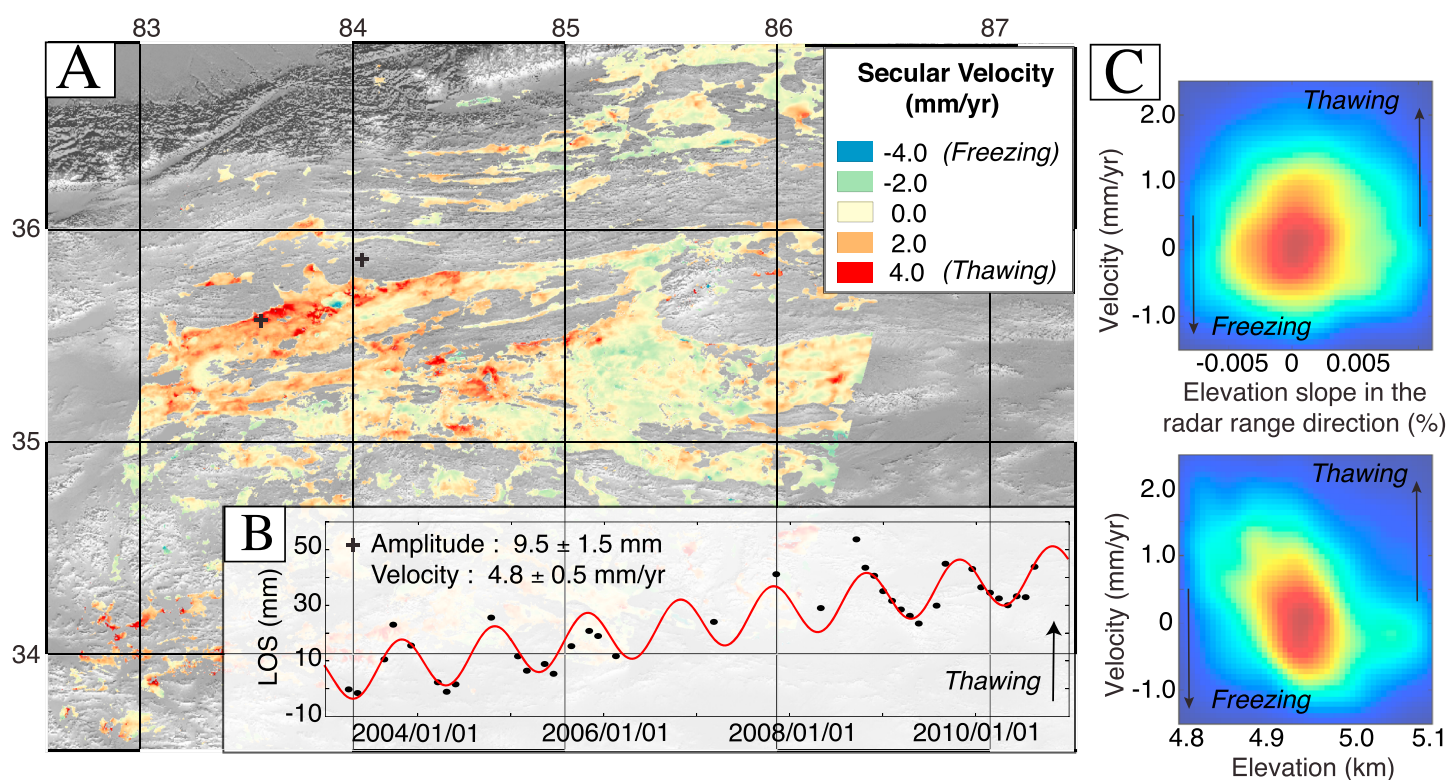
Figure 4. (a) Map of long-term ground velocity in line-of-sight (LOS) direction shown at pixels with amplitude of seasonal movement > 2.5 mm (Figure 1a). (b) Relative displacement time series with best fit sine functions between the two 5 × 5 pixels windows labeled by cross sign in Figure 4a. LOS increase represents ground subsidence. (c) Density plots showing correlation between multiannual trend and terrane slope along radar range direction (top) and elevation (bottom). Positive (negative) velocity indicates ice thawing (freezing).

than other tracks (Figures S2 and S11c). We rule out a significant contribution from horizontal movements to the LOS velocity (possible downslope movement of the soil due to gelifluction or frost creep) because the observed LOS velocity is mostly insensitive to the terrane slope direction (Figure 4c). The observed trend therefore suggests either a long-term ground subsidence (range increase) or uplift (range decrease).

The long-term temperature increase over Tibet from 2003 to 2011 is of 0.04–0.05°/yr [*Dee et al.*, 2011]. If the surface temperature was the sole controlling parameter of the velocity trend, it would affect the basins rather uniformly. However, we observe large spatial variations within basins in the long-term velocity map (Figure 4a). An ALT increase would primarily increase the amplitude of the seasonal oscillations, keeping constant the maximum uplift level during the winter season, a pattern that is not observed in the time series of individual pixels (Figure 4b). A possible explanation of lateral variations in the long-term ground displacement rate is the combined effects of basin drainage and ice loss due to temperature increase. In the case of drained sediments, the ice melting during the warm season should result in a water/ice volume loss in the soil, increasing the long-term subsidence rate. On the other hand, endorheic basins may collect more water during the thawing season than they loose by evaporation or percolation to greater depth, resulting in a long-term uplift trend.

We also observe a multiannual tendency toward thawing for lower elevation basins (Figure 4c), indicating a dependence to the ALT. Other specific ground conditions such as snow and vegetation cover may also influence the long-term trend. Further modeling would be necessary to assess the correlation of temperature increase, as well as these multiple parameters with regionally observed ground movement trend. For comparison, north of the Siling Co Lake in Central Tibet, at lower elevations and where the water content might not be the limiting factor to the permafrost related deformation, InSAR measurements indicate higher long-term subsidence rates than this study, reaching a centimeter per year [*Doin et al.*, 2015]. *Chang and Hanssen* [2015] measured vertical rates up to 10 mm/yr on the Qinghai-Tibet Railway, where the permafrost is there defined as sporadic [*Brown et al.*, 2000].

4. Conclusion

With an unprecedented spatial and temporal sampling, MT-InSAR data provide new insights into the dynamics of the permafrost active layer over a 60,000 km^2 area in northwestern Tibet. An 8 year timeline of the surface movement, sampling evenly the entire seasonal cycle reveals that the amplitude of the ground movements associated with the freeze-thaw cycle is strongly influenced by the nature of the terrain and the edaphic condition. Unconsolidated sediments in basins show larger amplitude of seasonal movement compared to exposed bedrock. Spatial variations of the amplitude and phase of the seasonal ground movements appear to be controlled by the ground water availability of the sediments rather than by the thickness of the active layer. Large ground oscillations (>8 mm) are observed over flat terrains in the centers of basins whereas smaller ground oscillations (2.5–8 mm) occur on slopes where less water is available in the soil. A degree-day integrated model adjusted to the data indicates that the subsidence that occurs during the period of diurnal temperature is superior to 0° over areas of large movement and that the pattern is delayed by 1–2 months for the areas of smaller movements. In addition to the seasonal signal, a multiannual trend of up to 3 mm/yr of subsidence is observed in limited areas and may be due to long-term changes in ground water supply and basin drainage. The recent launch of new SAR systems (Sentinel-1a/Sentinel-1b) with systematic acquisitions and shorter revisit time (down to 6 days) will allow scientists to better characterize the seasonal and interannual deformation response of the frozen ground to air temperature, solar radiation, and precipitation. Our study showed the potential of long temporal series of InSAR observations, opening new avenues of research on permafrost dynamics and climate.

References

Anderson, R. S., and S. P. Anderson (2010), *Geomorphology: The Mechanics and Chemistry of Landscapes*, Cambridge Univ. Press, Cambridge, U. K.

Berardino, P., G. Fornaro, R. Lanari, and E. Sansosti (2002), A new algorithm for surface deformation monitoring based on small baseline differential SAR interferograms, *IEEE Trans. Geosci. Remote Sens.*, *40*(11), 2375–2383.

Brown, J., K. Hinkel, and F. Nelson (2000), The circumpolar active layer monitoring (CALM) program: Research designs and initial results 1, *Polar Geogr.*, *24*(3), 166–258.

Chang, L., and R. Hanssen (2015), Detection of permafrost sensitivity of the Qinghai–Tibet railway using satellite radar interferometry, *Int. J. Remote Sens.*, *36*(3), 691–700.

Cheng, G., and T. Wu (2007), Responses of permafrost to climate change and their environmental significance, Qinghai–Tibet Plateau, *J. Geophys. Res.*, *112*, F02S03, doi:10.1029/2006JF000631.

Christensen, T. R., T. Johansson, H. J. Åkerman, M. Mastepanov, N. Malmer, T. Friborg, P. Crill, and B. H. Svensson (2004), Thawing sub-arctic permafrost: Effects on vegetation and methane emissions, *Geophys. Res. Lett.*, *31*, L04501, doi:10.1029/2003GL018680.

Daout, S., R. Jolivet, C. Lasserre, M.-P. Doin, S. Barbot, P. Tapponnier, G. Peltzer, A. Socquet, and J. Sun (2016), Along-strike variations of the partitioning of convergence across the Haiyuan fault system detected by InSAR, *Geophys J. Int.*, *205*(1), 536–547.

Dee, D., et al. (2011), The ERA-Interim reanalysis: Configuration and performance of the data assimilation system, *Q. J. R. Meteorol. Soc.*, *137*(656), 553–597.

Doin, M.-P., C. Lasserre, G. Peltzer, O. Cavalié, and C. Doubre (2009), Corrections of stratified tropospheric delays in SAR interferometriy: Validation with global atmospheric models, *J. Appl. Geophys.*, *69*, 35–50.

Doin, M.-P., F. Lodge, S. Guillaso, R. Jolvet, C. Lasserre, G. Ducret, R. Grandin, E. Pathier, and V. Pinel (2011), Presentation of the small baseline NSBAS Processing chain on a case example: The Etna deformation monitoring from 2003 to 2010 using Envisat data. paper presented at 2011 ESA Fringe, Frascati, Italy, 19–23 Sep.

Doin, M.-P., C. Twardzik, G. Ducret, C. Lasserre, S. Guillaso, and S. Jianbao (2015), InSAR measurement of the deformation around Siling Co Lake: Inferences on the lower crust viscosity in central Tibet, *J. Geophys. Res. Solid Earth*, *120*, 5290–5310, doi:10.1002/2014JB011768.

Ducret, G., M.-P. Doin, R. Grandin, C. Lasserre, and S. Guillaso (2014), DEM corrections before unwrapping in a Small Baseline Strategy for InSAR time series analysis, *IEEE Geosci. Remote Sens. Lett.*, *11*(1).

Fattahi, H., and F. Amelung (2014), InSAR uncertainty due to orbital errors, *Geophys. J. Int.*, *199*(1), 549–560.

Fort, M., and B. van Vliet-Lanoe (2007), Permafrost and periglacial environment of Western Tibet, *Landform Anal.*, *5*, 25–29.

French, H. M., M. Demitroff, S. L. Forman, and W. L. Newell (2007), A chronology of Late-Pleistocene permafrost events in southern New Jersey, Eastern USA, *Permafrost Periglac. Process.*, *18*(1), 49–59.

Gangodagamage, C., et al. (2014), Extrapolating active layer thickness measurements across Arctic polygonal terrain using LiDAR and NDVI data sets, *Water Resour. Res.*, *50*, 6339–6357, doi:10.1002/2013WR014283.

Grandin, R., M.-P. Doin, L. Bollinger, B. Pinel-Puysségur, G. Ducret, R. Jolivet, and S. N. Sapkota (2012), Long-term growth of the Himalaya inferred from interseismic InSAR measurement, *Geology*, *40*(12), 1059–1062.

Harlan, R., and J. Nixon (1978), Ground thermal regime, in *Geotechnical Engineering for Cold Regions*, edited by O. B. Andersland and D. M. Anderson, pp. 103–163, McGraw-Hill, New York.

Hinkel, K., J. Doolittle, J. Bockheim, F. Nelson, R. Paetzold, J. Kimble, and R. Travis (2001), Detection of subsurface permafrost features with ground-penetrating radar, Barrow, Alaska, *Permafrost Periglacial Process.*, *12*(2), 179–190.

Hooper, A., H. Zebker, P. Segall, and B. Kampes (2004), A new method for measuring deformation on volcanoes and other natural terrains using InSAR persistent scatterers, *Geophys. Res. Lett.*, *31*, L23611, doi:10.1029/2004GL021737.

Jolivet, R., R. Grandin, C. Lasserre, M.-P. Doin, and G. Peltzer (2011), Systematic InSAR tropospheric phase delay corrections from global meteorological reanalysis data, *Geophys. Res. Lett.*, *38*, L17311, doi:10.1029/2011GL048757.

Leppäranta, M. (1993), A review of analytical models of sea-ice growth, *Atmos. Ocean*, *31*(1), 123–138.

Liu, L., T. Zhang, and J. Wahr (2010), InSAR measurements of surface deformation over permafrost on the North Slope of Alaska, *J. Geophys. Res.*, *115*, F03023, doi:10.1029/2009JF001547.

Liu, L., K. Schaefer, T. Zhang, and J. Wahr (2012), Estimating 1992–2000 average active layer thickness on the Alaskan north slope from remotely sensed surface subsidence, *J. Geophys. Res.*, *117*, F01005, doi:10.1029/2011JF002041.

Liu, L., K. Schaefer, A. Gusmeroli, G. Grosse, B. M. Jones, T. Zhang, A. D. Parsekian, and H. A. Zebker (2014), Seasonal thaw settlement at drained thermokarst lake basins, Arctic Alaska, *Atmos. Chem. Phys.*, *8*(3), 815–826.

Liu, L., K. Schaefer, A. Chen, A. Gusmeroli, H. Zebker, and T. Zhang (2015), Remote sensing measurements of thermokarst subsidence using InSAR, *J. Geophys. Res. Earth Surf.*, *120*, 1935–1948, doi:10.1002/2015JF003599.

López-Quiroz, P., M.-P. Doin, F. Tupin, P. Briole, and J.-M. Nicolas (2009), Time series analysis of Mexico City subsidence constrained by radar interferometry, *J. Appl. Geophys.*, *69*(1), 1–15.

Lunardini, V. J. (1991), *Heat Transfer with Freezing and Thawing*, vol. 65, Elsevier, Amsterdam.

Nelson, F., N. Shiklomanov, G. Mueller, K. Hinkel, D. Walker, and J. Bockheim (1997), Estimating active-layer thickness over a large region: Kuparuk River basin, Alaska, USA, *Arct. Alp. Res.*, *29*, 367–378.

Oelke, C., and T. Zhang (2007), Modeling the active-layer depth over the Tibetan Plateau, *Arct. Antarct. Alp. Res.*, *39*(4), 714–722.

Outcalt, S. I., F. E. Nelson, and K. M. Hinkel (1990), The zero-curtain effect: Heat and mass transfer across an isothermal region in freezing soil, *Water Resour. Res.*, *26*(7), 1509–1516.

Pan, G.-T., J. Ding, D.-S. Yao, and L.-Q. Wang (2004), *Geological Map of the Qinghai-Xizang (Tibet) Plateau and Adjacent Areas*, Chengdu Cartographic, Chengdu, China.

Pastick, N. J., M. T. Jorgenson, B. K. Wylie, B. J. Minsley, L. Ji, M. A. Walvoord, B. D. Smith, J. D. Abraham, and J. R. Rose (2013), Extending airborne electromagnetic surveys for regional active layer and permafrost mapping with remote sensing and ancillary data, Yukon Flats Ecoregion, Central Alaska, *Permafrost Periglacial Process.*, *24*(3), 184–199.

Pinel, V., A. Hooper, D. la Cruz-Reyna, G. Reyes-Davila, and M. Doin (2008), Study of the deformation field of two active Mexican stratovolcanoes (Popocatepetl and Colima Volcano) by time series of InSAR data. paper presented at FRINGE 2007 Workshop, Frascati, Italy, 26–30 Nov.

Qingbai, W., L. Yongzhi, Z. Jianming, and T. Changjiang (2002), A review of recent frozen soil engineering in permafrost regions along Qinghai-Tibet Highway, China, *Permafrost Periglacial Process.*, *13*(3), 199–205.

Riseborough, D., N. Shiklomanov, B. Etzelmüller, S. Gruber, and S. Marchenko (2008), Recent advances in permafrost modelling, *Permafrost Periglacial Process.*, *19*(2), 137–156.

Rosen, P. A., S. Hensley, G. Peltzer, and M. Simons (2004), Updated repeat orbit interferometry package released, *Eos Trans. AGU*, *85*(5), 47–47.

Schaefer, K., L. Liu, A. Parsekian, E. Jafarov, A. Chen, T. Zhang, A. Gusmeroli, S. Panda, H. A. Zebker, and T. Schaefer (2015), Remotely sensed active layer thickness (ReSALT) at barrow, Alaska using interferometric synthetic aperture radar, *Remote Sens.*, *7*(4), 3735–3759.

Short, N., B. Brisco, N. Couture, W. Pollard, K. Murnaghan, and P. Budkewitsch (2011), A comparison of TerraSAR-X, RADARSAT-2 and ALOS-PALSAR interferometry for monitoring permafrost environments, case study from Herschel Island, Canada, *Remote Sens. Environ.*, *115*(12), 3491–3506.

Smith, M., and D. Riseborough (1996), Permafrost monitoring and detection of climate change, *Permafrost Periglacial Process.*, *7*(4), 301–309.

Stefan, J. (1891), Über die theorie der eisbildung, insbesondere über die eisbildung im polarmeere, *Ann. Phys.*, *278*(2), 269–286.

Strozzi, T., and U. Wegmuller (1999), Land subsidence in Mexico City mapped by ERS differential SAR interferometry. paper presented at IEEE 1999 International Geoscience and Remote Sensing Symposium, 1999. IGARSS'99 Proceedings, vol. 4, pp. 1940–1942, IEEE.

Wu, Q., T. Zhang, and Y. Liu (2010), Permafrost temperatures and thickness on the Qinghai-Tibet Plateau, *Global Planet. Change*, *72*(1), 32–38.

Yun, S.-H., H. Zebker, P. Segall, A. Hooper, and M. Poland (2007), Interferogram formation in the presence of complex and large deformation, *Geophys. Res. Lett.*, *34*, L12305, doi:10.1029/2007GL029745.

Zhang, L., X. Ding, Z. Lu, H.-S. Jung, J. Hu, and G. Feng (2014), A novel multitemporal InSAR model for joint estimation of deformation rates and orbital errors, *IEEE Trans. Geosci. Remote Sens.*, *52*(6), 3529–3540.

Zorigt, M., J. Kwadijk, E. Van Beek, and S. Kenner (2016), Estimating thawing depths and mean annual ground temperatures in the Khuvsgul region of Mongolia, *Environ. Earth Sci.*, *75*(10), 1–10.